Supporting Information

for

Jet aircraft lubrication oil droplets as contrail ice-forming particles

Joel Ponsonby[1], Leon King[2], Benjamin J. Murray[2] and Marc E. J. Stettler[1*]

[1]Department of Civil and Environmental Engineering, Imperial College London, London, SW7 2AZ, United Kingdom
[2]School of Earth and Environment, University of Leeds, Woodhouse, Leeds, LS2 9JT, United Kingdom

**Correspondence to*: Marc Stettler (m.stettler@imperial.ac.uk)

Contents

S1 Chamber Characterisation

Before performing expansion measurements using the lubrication oil, the experimental setup was characterised. First, the aerosol chamber was cleaned using a continual flow of compressed air at a rate of 2 L min^{-1} over 78 hours (~9 equivalent volume replacements). The particle sizing apparatus was then used to estimate the size distribution for the chamber background.

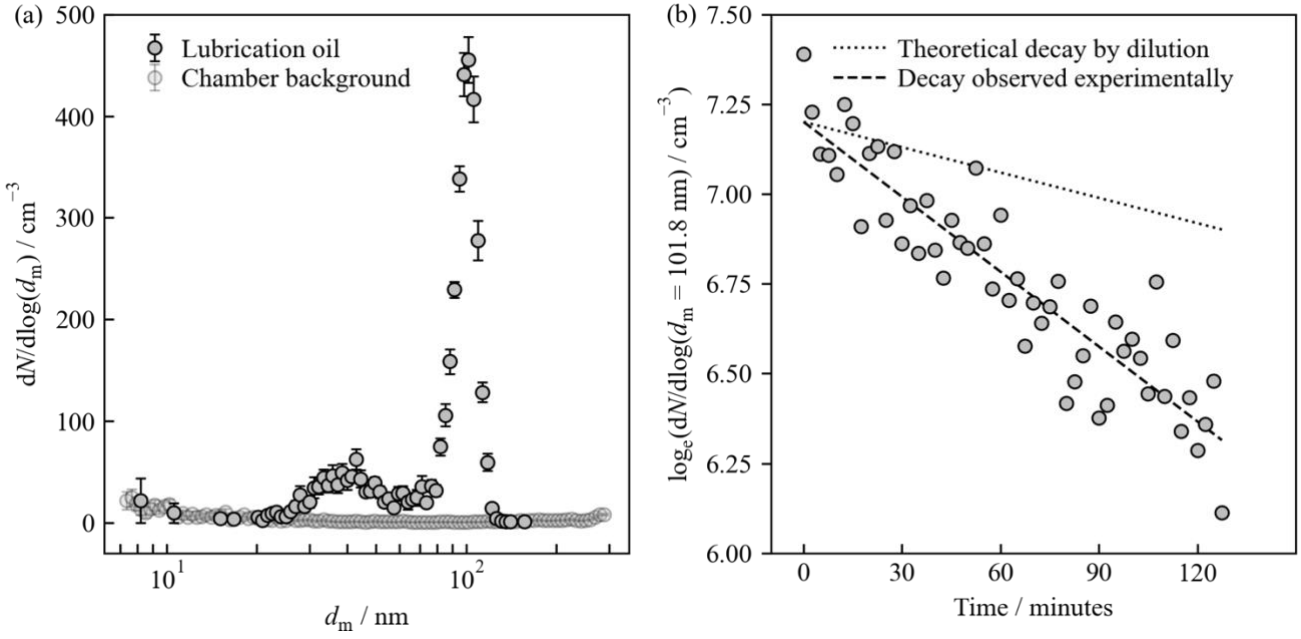

Figure S1: (a) Size distribution measurements within the aerosol chamber after it was cleaned (hollow markers) and after it was "primed" with lubrication oil droplets (grey markers). (b) Chamber concentration of lubrication oil droplets with d_m = 101.8 nm as a function of time during a typical measurement (grey markers). Fitted concentration decay (dashed line) (half-life of 100 ± 6 min) was compared to a theoretical decay accounting for dilution (dotted line) (half-life of 294 min).

The background size distribution is shown in Fig. S1. This is compared to the size distribution recorded for a typical lubrication oil sample at the AAC output. The number concentration recorded at the AAC output for d_m ~100 nm is over two orders of magnitude greater than the background chamber number concentration. Therefore, it is reasonable to neglect background contributions at d_m ~100 nm when examining particle size distributions obtained using the particle sizing apparatus.

Particle losses within the chamber were also investigated. During measurements with the lubrication oil droplets, compressed air was fed into the chamber at 2.35 L min^{-1}. Of this, 1 L min^{-1} was directed towards the particle sizing apparatus and 1.35 L min^{-1} was directed towards the AAC and PINE chamber. Theoretically, the reduction in chamber concentration due to chamber dilution should therefore follow a first-order exponential decay with a half-life of 294 min (dotted line), see Fig. S1b. Estimated sedimentation losses of d_m = 101.8 nm particles within the chamber were negligible over this timescale. With a newly "primed" chamber, the concentration of particles with electrical mobility diameters of d_m = 101.8 nm was monitored. The temporal reduction in concentration was found to follow a first-order exponential decay (dashed line) with a half-life of (100 ± 6) min, see Fig. S1b. This suggests that other loss mechanisms were in effect within the dilution timescale,

although the source and relative significance of these processes was not investigated further. Instead, to mitigate concentration reductions, the chamber was "primed" approximately every 100 minutes.

S2 AAC Transfer Function

This section outlines the key steps and equations necessary to derive the AAC transfer function and characterise its dependencies. These were reproduced from (Johnson et al., 2018) and its associated supplemental material; for a complete and detailed derivation of the AAC transfer function, the reader is directed towards these texts. The AAC separates particles according to the particle relaxation time, τ, which is a function of the aerodynamic diameter, d_a, according to (Johnson et al., 2018)

$$\tau = \frac{C_c(d_a)\rho_0 d_a^2}{18\mu}, \tag{S1}$$

where $C_c(d_a)$ is the Cunningham slip correction factor, ρ_0 is the unit density and μ is the viscosity of the surrounding medium. It has been demonstrated that the particle relaxation time selected by the AAC, τ^*, can be expressed as (Johnson et al., 2018)

$$\tau^* = \frac{Q_{sh} + Q_{exh}}{\pi\omega^2(r_1+r_2)^2 L}, \tag{S2}$$

where Q_{sh} and Q_{exh} are the respective sheath flows entering and leaving the classifier, L is the classifier effective length, r_1 and r_2 are the inner and outer classifier radii and ω is the classifier rotational speed. To account for particle losses within the classifier, a transfer function width factor $\mu(d_a)$ and transmission efficiency λ can be defined, which scale transfer function width and area respectively (Johnson et al., 2018). Using these scaling parameters, the theoretical AAC transfer function is described by the quasi-triangular distribution (Johnson et al., 2018)

$$\mathrm{F}(\tau, \tau^*, \mu, \lambda, \beta) = \begin{cases} \lambda\mu\left[1+\frac{\mu}{\beta}\left(\frac{\tau}{\tau^*}-1\right)\right] & \text{if } \left(1-\frac{\beta}{\mu}\right)\tau^* \le \tau \le \tau^* \\ \lambda\mu\left[1+\frac{\mu}{\beta}\left(1-\frac{\tau}{\tau^*}\right)\right] & \text{if } \tau^* < \tau \le \left(1+\frac{\beta}{\mu}\right)\tau^* \\ 0 & \text{otherwise} \end{cases}, \tag{S3}$$

where, for balanced inlet (Q_{in}) and outlet (Q_{out}) flows and $Q_{sh} = Q_{exh}$, β is given by the ratio of Q_{in} to Q_{sh}.

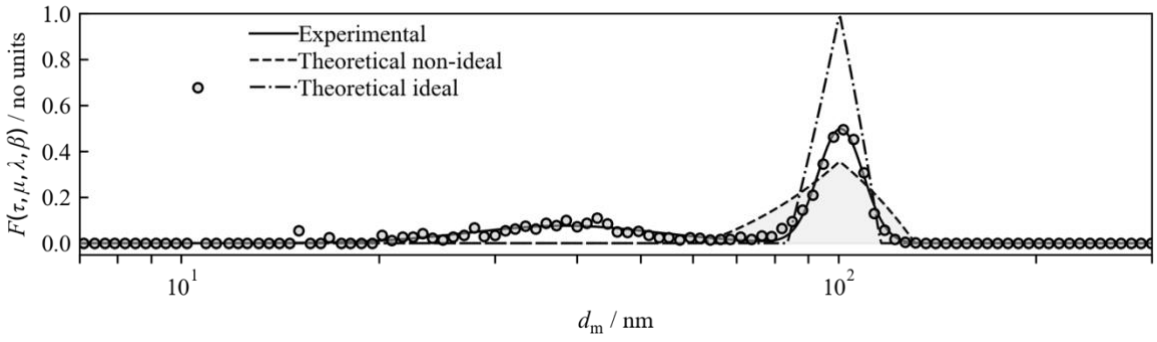

Figure S2: The experimental AAC transfer function (grey markers) explicitly derived using experiments described in Sect. 3.4 of the main text, with parameters (ω, r_1, r_2, L, Q_{sh}, Q_{in}) of (488.7 rad s^{-1}, 0.056 m, 0.06 m, 0.206 m, 5.14 L min^{-1}, 1.05 L min^{-1}). This has been fitted to a bimodal lognormal distribution (solid line) with secondary and primary modes characterised by (GSD, d_m / nm) of (1.39 ± 0.11, 38.3 ± 3.0) and (1.09 ± 0.01, 100.9 ± 0.6) respectively. Using the same parameters, the non-ideal AAC transfer function (accounting for particle losses) has been plotted (dashed line), where λ = 0.8 (Johnson et al., 2018) and $\mu = \mu(d_a)$ according to the parametrization outlined in (Birmili et al., 1997). Finally, the ideal (lossless) AAC transfer function has also been plotted with $\lambda = \mu$ =1 (dot-dash-dot line).

The experimental transfer function obtained using experiments outlined in the main text (Sect. 3.4) is presented alongside the two theoretical AAC transfer functions, corresponding to ideal and non-ideal parametrizations. Using Fig. S2, the area under the experimental transfer function is comparable to that of the non-ideal theoretical parametrization, albeit with a narrower width that more closely resembles the ideal theoretical parametrization. The experimental transfer distribution exhibits a primary mode at d_m = (100.9 ± 0.6) nm, expected based on the theoretical distributions. A less significant secondary mode at a GMD d_m = (38.3 ± 3.0) nm is also visible, which has an integrated concentration that is approximately two-thirds that of the first mode. During expansion measurements, the larger particle mode at a GMD d_m = (100.9 ± 0.6) nm will activate in preference to the secondary mode at d_m = (38.3 ± 3.0) nm. Therefore, for the purposes of activation measurements, the experimental transfer function in Fig. S2 can be effectively considered as a single particle mode at d_m = (100.9 ± 0.6) nm.

S3 Relative Humidity Calculations and Uncertainty Analysis

For each expansion measurement, three parameters are required to generate (T_o, $RH_{i,o}$) estimates and populate the phase space in Fig. 1, within the main text. The first parameter is the temperature within the PINE chamber immediately before an expansion measurement, T_i. This parameter is bounded by instrumental resolution at ΔT_i = ± 0.1 K. The second and third parameters are the chamber pressures immediately before an expansion and at onset, $P_{i,C}$ and $P_{o,C}$ respectively. Uncertainties associated with these pressure values, $\Delta P_{i,C}$ and $\Delta P_{o,C}$, were obtained as described in the main text (Sect. 4.1). Using these three parameters, (T_o, RH_i) can be estimated for a given expansion provided that two criteria are met. Firstly, it is assumed that prior to an expansion, sample aerosol flowing through the PINE system reaches equilibrium with the chamber walls. This means that the sample aerosol before an expansion measurement is at RH_i = 100%, such that the initial gas-phase water partial pressure is equal to the vapour pressure above ice, $p_{i,w} = p_{i,ice}$. Secondly, it is assumed that the chamber expands adiabatically so that the onset temperature, T_o, can be derived using the relation (Pruppacher and Klett, 2010)

$$T_o = T_i \left(\frac{P_{i,C}}{P_{o,C}}\right)^{\frac{1-\gamma}{\gamma}}, \tag{S4}$$

where γ is the adiabatic index for air. The vapour pressure above ice is a function of temperature alone (Murphy and Koop, 2005), therefore once the value of T_o has been obtained using Eq. (S4), both the onset and initial vapour pressures above ice can be determined. The initial and onset vapour pressures above ice, $p_{i,ice}$ (T_i) and $p_{o,ice}$ (T_o) respectively, can then be combined with the chamber pressures to derive the value of $RH_{i,o}$ according to

$$RH_{i,o} = \frac{p_{o,w}}{p_{o,ice}} = \frac{p_{i,ice}(T_i)}{p_{o,ice}(T_i, P_{i,C}, P_{o,C})} \frac{P_{o,C}}{P_{i,C}}. \tag{S5}$$

Therefore, using the measured values of $P_{o,C}$, $P_{i,C}$ and T_i, the position (T_o, $RH_{i,o}$) can be estimated for a given expansion. For an individual expansion, the uncertainty in the position (T_o, $RH_{i,o}$) was derived by propagating uncertainties $\Delta P_{i,C}$, $\Delta P_{o,C}$ and ΔT_i through the following implicit relations

$$\Delta T_o^2 = \left(\frac{\partial T_o}{\partial P_{i,C}}\right)^2 \Delta P_{i,C}^2 + \left(\frac{\partial T_o}{\partial P_{o,C}}\right)^2 \Delta P_{o,C}^2 + \left(\frac{\partial T_o}{\partial T_i}\right)^2 \Delta T_i^2 , \quad \text{(S6)}$$

$$\Delta RH_{i,o}^2 = \left(\frac{\partial RH_{i,o}}{\partial T_i}\right)^2 \Delta T_{i,}^2 + \left(\frac{\partial RH_{i,o}}{\partial P_{o,C}}\right)^2 \Delta P_{o,C}^2 + \left(\frac{\partial RH_{i,o}}{\partial P_{i,C}}\right)^2 \Delta P_{i,C}^2 . \quad \text{(S7)}$$

Note that explicit forms of Eq. (S6) and Eq. (S7) were derived using Eq. (S4) and Eq. (S5) as well as the vapour pressure parametrization outlined by Murphy and Koop (Murphy and Koop, 2005). Expansions that were performed at similar temperatures were subsequently averaged to produce Fig. 4b (in the main text). For completeness, to determine the uncertainty, $\overline{\Delta RH}_{i,o}$, for a series of n expansions, the following expression was used

$$\overline{\Delta RH}_{i,o}^2 = \frac{1}{n}\left[\Delta RH_{i,o}^2(n=1) + \Delta RH_{i,o}^2(n=2) + \ldots \Delta RH_{i,o}^2(n=n)\right] . \quad \text{(S8)}$$

S4 Droplet activation and κ-Köhler Theory

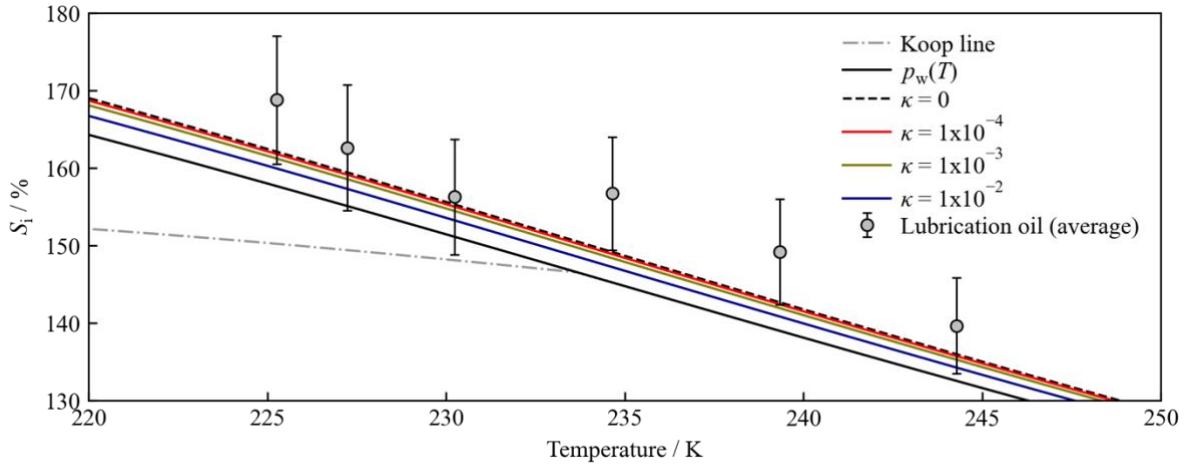

Figure S3: Average lubrication oil onset positions are compared to the water saturation line, $p_w(T)$, and κ-isolines at various values of κ. The Koop line is also plotted (Koop et al., 2000).

Activation of liquid droplets may be described using κ-Köhler theory, which ascribes each material with a hygroscopicity parameter κ (Petters and Kreidenweis, 2007). This parameter is related to the critical supersaturation required for droplet activation, which is the saturation required to activate half of the CN (Krüger et al., 2014; Koehler et al., 2009; Pound, 1972). A more hygroscopic material will have a higher value of κ and will activate at a lower critical supersaturation (Petters and Kreidenweis, 2007) . The upper limit for a hygroscopic aerosol (i.e., NaCl) is κ ~1.1 (Zieger et al., 2017). On the other hand, materials with κ that approach 0 are said to be non-hygroscopic; these require appreciably larger critical supersaturations in order to activate and are therefore less active as CN (Petters and Kreidenweis, 2007). Using Fig. S3, the onset positions for lubrication oil droplets are shown to be consistent with a hygroscopicity parameter of 0.

S5 Expansion Particle Size Distributions

The number concentration recorded by the OPC during each expansion was used to infer the ice nucleation mechanism in the main text (Sect. 4.2). Fig. S4 was produced by integrating over Fig. 5 (in the main text) in temperature (i.e., over the entire duration of the expansion), enabling GMDs to be fitted for both monomodal and bimodal lognormal distributions.

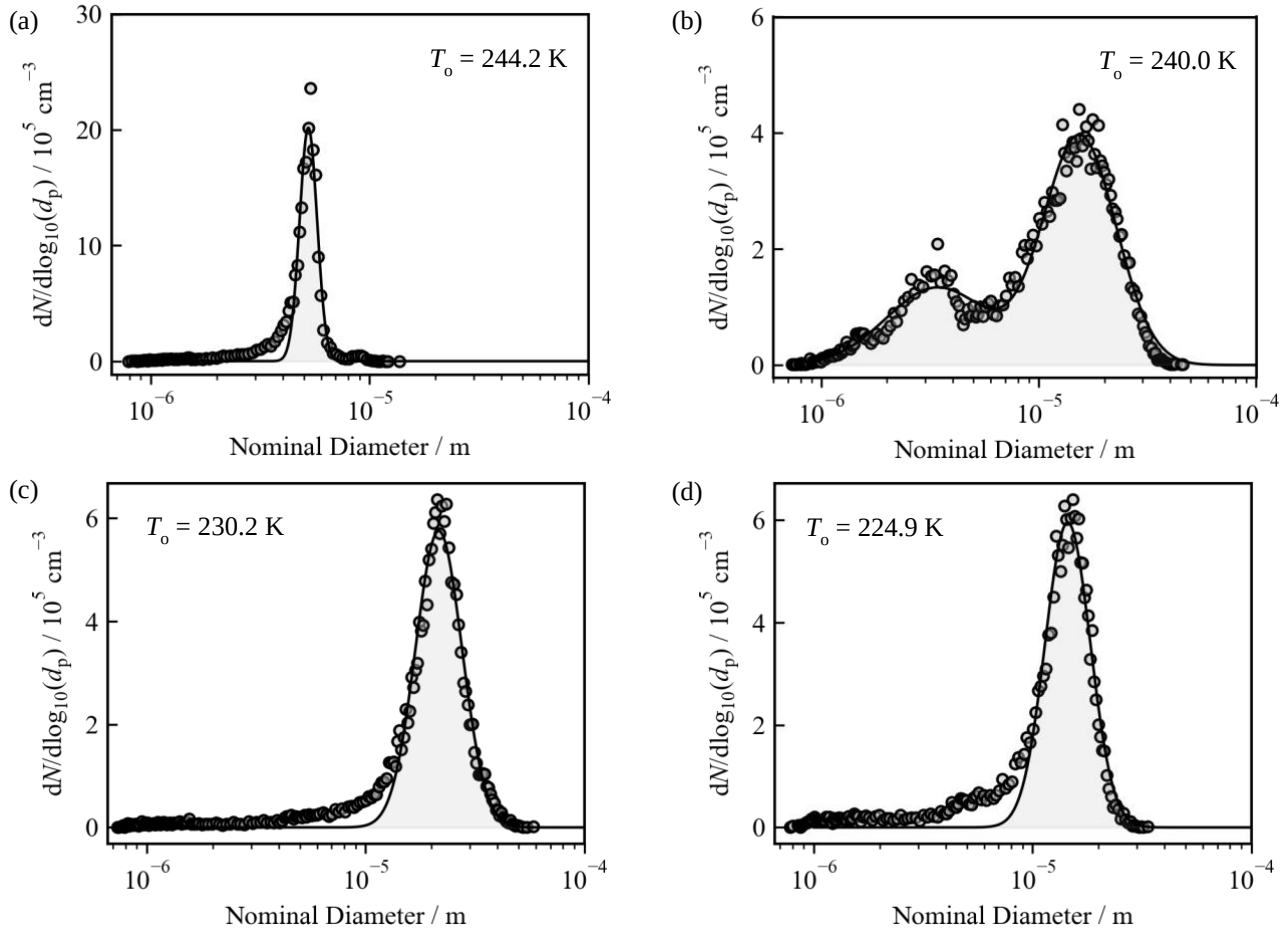

Figure S4: Fitted integrated nominal particle size distributions for expansions at onset temperatures of (a) 244.2 K (b) 240.0 K (c) 230.2 K (d) 224.9 K. These are reduced representations of Fig. 5 (in the main text), as integrations over temperature.

S6 Estimating the Homogeneous Nucleation Temperature

To estimate the homogeneous nucleation temperature for a collection of cooling water droplets, the droplet size distribution and cooling profile *T(t)* (the temperature as a function of time) are required. First, the homogeneous nucleation rate coefficient *J(t)* can be determined at any point during the cooling profile using the best-fit parametrization outlined by Murray and Koop (Koop and Murray, 2016). This is a function of temperature alone and agrees with classical nucleation theory to within 1.3% for temperatures in the range 230 - 245 K. Note that for a given cooling profile, the homogeneous nucleation temperature can equally be parametrized in *t*. Next, the expected number of droplets to freeze after a given time, *N(t)*, can be calculated using the relation outlined by Murray et al (Murray et al., 2010). This depends exponentially on *J*, *t* and the droplet volume. The fraction of droplets which are expected to homogeneously freeze after a given time, *f(t)*, can then be determined by dividing *N(t)* by the total number of droplets. Finally, *f(T)* can be plotted as a function of *T* to examine under what conditions the sample nucleates ice homogeneously.

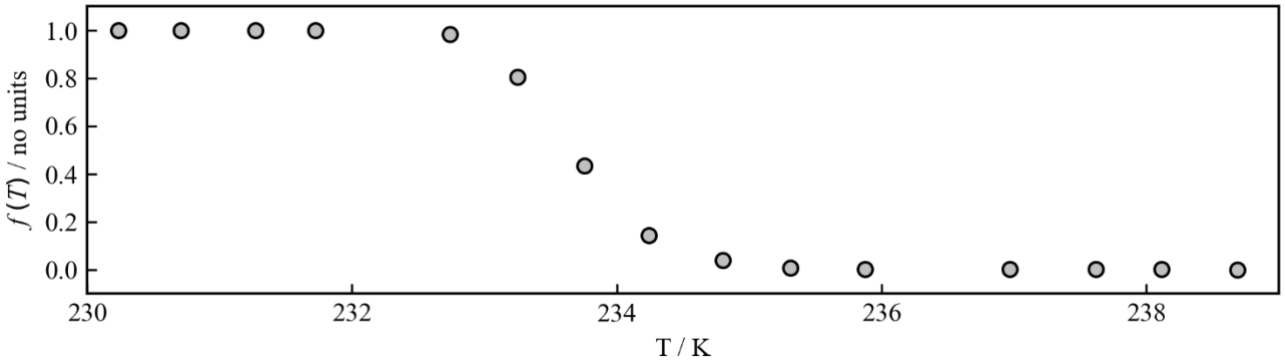

Figure S5: Fraction of droplets freezing homogeneously as a function of temperature *f*(*T*) for the experimental data shown in Fig. 5b (in the main text). The size distribution of droplets was estimated using lognormal fit parameters obtained using Fig. 5a (in the main text). The *f*(*T*) profile was then produced with grey markers at each of the temperature intervals recorded in the *T*(*t*) profile. Using the markers, the onset of homogeneous nucleation was estimated as ~235 K.

To estimate the homogeneous nucleation temperature based on experimental data in Fig. 5b (in the main text), the discrete experimental cooling profile *T(t)* and the size distribution of liquid water droplets were required. The cooling profile was obtained by calculating the adiabatic temperature at each point during the expansion, using Eq. (S5). The size distribution of liquid droplets was estimated using the parameters identified for the fitted size distribution in Fig. 5a (in the main text). As discussed in the main text (Sect. 4.2), this reflects the size distribution of water droplets that form on lubrication oil droplets. During analysis, the total droplet volume occupied by the lubrication oil droplets was neglected as the diameter of the water droplets observed in Fig. 5a (in the main text) were several orders of magnitude larger than the diameter of lubrication oil droplets. As in a monodisperse system, *T(t)* was used to estimate *J(t)* at each time interval during the cooling profile. Next, the droplet size distribution was discretized into infinitesimally narrow bins, within which the droplet volume was fixed. For each bin *i*, the expected number of droplets freezing homogeneously, *n(t, i)*, was estimated at each time interval during the cooling profile. Finally, at each time interval, *n(t, i)* values were integrated across each bin (to produce *N(t)*) and divided by the total number concentration, reproducing an *f(t)* profile. This profile has been parametrized in temperature to produce Fig. S5, from which the *onset* of homogeneous nucleation is estimated as ~235 K.

References

Birmili, W., Stratmann, F., Wiedensohler, A., Covert, D., Russell, L. M., and Berg, O.: Determination of Differential Mobility Analyzer Transfer Functions Using Identical Instruments in Series, Aerosol Science and Technology, 27, 215–223, https://doi.org/10.1080/02786829708965468, 1997.

Johnson, T. J., Irwin, M., Symonds, J. P. R., Olfert, J. S., and Boies, A. M.: Measuring aerosol size distributions with the aerodynamic aerosol classifier, Aerosol Science and Technology, 52, 655–665, https://doi.org/10.1080/02786826.2018.1440063, 2018.

Kärcher, B., Burkhardt, U., Bier, A., Bock, L., and Ford, I. J.: The microphysical pathway to contrail formation, J Geophys Res, 120, 7893–7927, https://doi.org/10.1002/2015JD023491, 2015.

Koehler, K. A., DeMott, P. J., Kreidenweis, S. M., Popovicheva, O. B., Petters, M. D., Carrico, C. M., Kireeva, E. D., Khokhlovac, T. D., and Shonijac, N. K.: Cloud condensation nuclei and ice nucleation activity of hydrophobic and hydrophilic soot particles, Physical Chemistry Chemical Physics, 11, 7906–7920, https://doi.org/10.1039/b916865f, 2009.

Koop, T. and Murray, B. J.: A physically constrained classical description of the homogeneous nucleation of ice in water, Journal of Chemical Physics, 145, 211915, https://doi.org/10.1063/1.4962355, 2016.

Koop, T., Beiping, L., Tsias, A., and Peter, T.: Water activity as the determinant for homogeneous ice nucleation in aqueous solutions, Nature, 406, 611–614, https://doi.org/https://doi.org/10.1038/35020537, 2000.

Krüger, M. L., Mertes, S., Klimach, T., Cheng, Y. F., Su, H., Schneider, J., Andreae, M. O., Pöschl, U., and Rose, D.: Assessment of cloud supersaturation by size-resolved aerosol particle and cloud condensation nuclei (CCN) measurements, Atmos Meas Tech, 7, 2615–2626, https://doi.org/10.5194/amt-7-2615-2014, 2014.

Murray, B. J., Broadley, S. L., Wilson, T. W., Bull, S. J., Wills, R. H., Christenson, H. K., and Murray, E. J.: Kinetics of the homogeneous freezing of water, Physical Chemistry Chemical Physics, 12, 10380–10387, https://doi.org/10.1039/c003297b, 2010.

Petters, M. D. and Kreidenweis, S. M.: A single parameter representation of hygroscopic growth and cloud condensation nucleus activity, Atmos Chem Phys, 7, 1961–1971, https://doi.org/10.5194/acp-7-1961-2007, 2007.

Pound, G. M.: Selected Values of Critical Supersaturation for Nucleation of Liquids from the Vapor, J Phys Chem Ref Data, 1, 119–133, https://doi.org/10.1063/1.3253095, 1972.

Pruppacher, H. R. and Klett, J. D.: Cooling of Moist Air, in: Microphysics of Clouds and Precipitation, Springer Dordrecht, 485–501, https://doi.org/10.1007/978-0-306-48100-0, 2010.

Zieger, P., Väisänen, O., Corbin, J. C., Partridge, D. G., Bastelberger, S., Mousavi-Fard, M., Rosati, B., Gysel, M., Krieger, U. K., Leck, C., Nenes, A., Riipinen, I., Virtanen, A., and Salter, M. E.: Revising the hygroscopicity of inorganic sea salt particles, Nat Commun, 8, https://doi.org/10.1038/ncomms15883, 2017.